Frontal Interaction with Mesoscale Topography

MICHAEL J. DICKINSON AND DAVID J. KNIGHT

Department of Earth and Atmospheric Sciences, The University at Albany, State University of New York, Albany, New York

(Manuscript received 18 November 1997, in final form 15 January 1999)

ABSTRACT

A two-dimensional, hydrostatic, nearly adiabatic primitive equation model is used to study the evolution of a front passing across topography. Frontogenesis is forced by shearing deformation associated with the nonlinear evolution of an Eady wave. This study extends previous work by including an upper-level potential vorticity (PV) anomaly and a growing baroclinic wave in a baroclinically unstable basic state.

Results for the Eady wave simulations show that the mountain retards and blocks the approaching front at the surface while the upper-level PV anomaly associated with the front moves across the domain unaffected. Warm advection ahead of the lee trough forces convergence and cyclonic vorticity growth near the base of the lee slope. This vorticity growth is further encouraged by the approach of the upper-level PV anomaly. The upper-level PV anomaly then couples with this new surface vorticity center and propagates downstream. The original surface front remains trapped on the windward slope. Thus when the upstream blocking is strong, frontal propagation is discontinuous across the ridge. This evolution occurs for tall mountains and narrow mountains, as well as weak fronts. For low mountains, wide mountains, and strong fronts, only weak retardation is observed on the windward slope. The surface front remains coupled with the upper-level PV anomaly. The front moves continuously across the mountain.

The net result, regardless of mountain size and shape, is that the front reaches the base of the lee slope stronger, sooner, and with a decreased cross-front scale compared to the ''no-mountain'' case. Well downstream of the mountain, no position change of the surface front is observed.

1. Introduction

The interaction of fronts with terrain has been a long standing problem confronting both synoptic and dynamic meteorologists. The idea that mountains impeded frontal propagation and deformed frontal zones was known to the Bergen school in the early 1920s. Detailed observations of frontal retardation and distortion by mountains were first illustrated by Bjerknes and Solberg (1922). Much of the recent observational information of front–mountain interactions can be attributed to the Alpine Experiment (ALPEX) (e.g., Hoinka and Volkert 1987), which was designed, in part, to investigate lee cyclogenesis in the Alpine region. More recently, O'Handley and Bosart (1996) and Schumacher et al. (1996) performed a climatology of cold fronts aligned parallel to and moving toward the Appalachian Mountains.

Attempts to understand the propagation of fronts across terrain have focused on analytical and numerical model solutions. Excellent reviews of previous work are presented by Blumen (1992) and Egger and Hoinka (1992).

Deformation-forced fronts interacting with terrain have been considered by Bannon (1983, 1984), Zehnder and Bannon (1988, hereafter ZB88), Williams et al. (1992, hereafter W92), and Keuler et al. (1992, hereafter K92). Deformation-forced fronts exhibit a time-dependent ageostrophic circulation. These deformation models employed a uniform background flow, constant static stability, smooth mountain slopes, and prescribed deformation forcing. These studies show that fronts are slowed and weakened by the mountain circulation along the windward slope, consistent with the observational studies of Hartsough and Blumen (1990) and Schumacher et al. (1996). Acceleration and rapid intensification of the front are observed along the lee slope.

There is little agreement, however, concerning the net effect of the front–mountain interaction. ZB88 found that the surface front is slightly weaker and is displaced approximately 100 km farther downstream after the mountain interaction compared to the no-mountain simulation. Conversely, K92 showed that the surface front is stronger downstream of the lee slope. The results of W92 showed no net change in frontal strength or position after the interaction. These differences were addressed by Egger and Hoinka (1992), who note that the numerical model used in ZB88 requires an ageostrophic

Corresponding author address: Michael J. Dickinson, Department of Earth and Atmospheric Sciences, The University at Albany, State University of New York, 1400 Washington Ave., Albany, NY 12222. E-mail: mjd@atmos.albany.edu

outflow to balance mass, which may affect frontogenesis within the model. In addition, the use of a rigid upper boundary in ZB88 and W92 results in an artificial net turning of the flow. The study of K92 employed an open upper boundary, allowing strong stationary mountain waves to persist aloft. K92 speculated that these waves enhanced frontogenesis along the lee slope.

Apart from K92, previous studies have not employed vertical wind shear in the basic state, contrary to midlatitude frontal cyclone environments. Numerical modeling studies by Bannon and Zehnder (1989) have shown that baroclinic flow over a ridge produces weaker along-mountain jets and a weaker mountain anticyclone compared to the barotropic case. As a result, the mountain circulation and subsequent frontal retardation may be strongly influenced by the inclusion of basic-state baroclinicity.

K92 extend previous studies by employing a linear vertical shear flow to force frontogenesis in their model. In the lee of the mountain, a rapid strengthening of the temperature gradient is observed. This increased frontogenesis in the lee of the mountain is produced through differential meridional temperature advection, not present in deformation models. In addition, the downslope flow in the shear case was larger than in the deformation case leading to increased convergence and frontogenesis. K92 suggests that the progression of the surface front across the ridge is a discontinuous process. In other words, the original surface front remains trapped along the windward slope while a new, independent surface front forms on the lee slope and becomes the dominant feature. A similar result was shown observationally by Kurz (1990). K92 suggest that the discontinuous propagation results from the interaction of the front with the mountain wave.

In the real atmosphere, active fronts form in conjunction with upper-level jet streaks or positive PV anomalies associated with a growing baroclinic wave (Keyser 1986). This upper-level feature has been represented in the two-dimensional shallow water studies of Egger (1995). It has not, however, been represented in previous two-dimensional primitive equation modeling studies. The present study investigates front–mountain interactions in which an upper-level potential vorticity (PV) anomaly and a baroclinic basic state are included in a two-dimensional primitive equation model by examining the development of a dry, inviscid, nonlinear Eady wave (Eady 1949). Frontogenesis is forced by the nonlinear evolution of the Eady wave. Though this may not be the best representation of a midlatitude frontal structure, the Eady wave is the simplest basic state that supports baroclinic growth.

A primitive equation model permits the generation of inertia-gravity waves, which are not allowed in quasi-geostrophic or semigeostrophic models. With inertia-gravity waves the mountain circulation is no longer symmetric about the terrain, which may influence frontogenesis.

The Eady wave solution has uniform interior PV. The upper-level PV anomaly in the Eady model is supplied by potential temperature anomalies on the upper boundary. The inclusion of the upper-level PV anomaly supports the presence of an along-jet transverse circulation, with ascent east and descent west of the upper-level positive PV anomaly. The lower branch of the circulation is oriented in the direction of the moving front. Schumacher et al. (1996) hypothesizes that these circulations may supply additional impetus to allow the front to cross the ridge.

Section 2 describes the model and parameters used in this study. Model initialization is presented in section 3. Results for the control simulations are presented in section 4. Results for the sensitivity studies, in which mountain size and frontal strength are changed, are presented in section 5. Finally, section 6 contains a discussion and conclusions from this study.

2. Model description

The model employed in this study is a two-dimensional version of the National Center for Atmospheric Research Pennsylvania State University (NCAR–PSU) primitive equation mesoscale model, first described by Anthes and Warner (1978). The model has been adapted by Keyser and Anthes (1982) to study the evolution of a finite-amplitude Eady wave according to the shear model of frontogenesis of Hoskins and Bretherton (1972, hereafter HB72). The model is taken to be inviscid except for parameterized diffusion. In addition, surface heat and moisture fluxes are neglected.

The Keyser and Anthes version of the NCAR–PSU model is hydrostatic and compressible. The model atmosphere is bounded from above by a constant pressure surface (p_t) and from below by a rigid boundary with terrain elevation varying in the x direction only, and surface pressure p_s varying in both the x and y directions. The model uses the primitive equations in terrain-following sigma (σ) coordinates, where σ is defined as

$$\sigma = \frac{p - p_t}{p^*}, \tag{1}$$

where $p^* = p_s - p_t$. The upper and lower boundaries are constrained so that the vertical velocity is zero. Sloping terrain and $\dot{\sigma} = 0$ implies that the vertical velocity in height coordinates, given by $w = dz/dt$, is equal to $u(dh/dx)$, where u is the along-slope velocity and dh/dx is the slope of the terrain. This results in a fully nonlinear lower boundary condition.

The three-dimensional primitive equations given in Anthes and Warner (1978) can be expressed in two-dimensional form by specifying the y dependence (i.e., north–south direction) of the variables u, v, T, and p^*. The terrain slope in the north–south direction is zero. The meridional gradients of u and v are taken to be zero on constant σ surfaces. The meridional gradients of p^* and T are analytically determined from the geostrophic

TABLE 1. List of model parameters used in this study.

Parameter	Numerical value	Parameter	Numerical value
Δt	15 s	$\partial\theta/\partial z$	3.5 K km^{-1}
Δx	17.5 km	H	1 km
P_t	308 hPa	L	500 km
P_o	1000 hPa	f	1.0×10^{-4} s^{-1}
C	8.0 m s^{-1}		

and thermal winds, respectively, of the Eady problem. When these constraints are substituted into the full three-dimensional equations, the two-dimensional equations are obtained. For complete derivation of the model equations, the reader is referred to Keyser and Anthes (1982).

The model terrain has the form

$$h = \begin{cases} 0 & x < -L,\ x > L \\ H\cos^2\left(\dfrac{\pi x}{2L}\right) & -L \le x \le L, \end{cases} \tag{2}$$

where H is the height of the mountain, L is the mountain half-width, and $x = 0$ at the center of the domain and increases eastward. The parameters for the control case are presented in Table 1. To reduce the effect of short wavelength numerical noise, a fourth-order horizontal diffusion scheme is employed. The background diffusion coefficient, which is dependent on the grid spacing, is made just large enough to damp numerical noise.

In addition, a layer of enhanced second-order diffusion is located at the upper boundaries. The use of a second-order diffusion prevents gravity waves from reaching and reflecting off the upper boundary back into the domain. The upper absorbing layer has negligible effect on the development of the Eady wave. The reader is referred to Dickinson (1995, hereafter D95) for a detailed description of the diffusion used in this study.

Time integration in the model follows the method of Brown and Campana (1978). This scheme averages the pressure gradient term and yields results similar to the standard leapfrog scheme, while allowing for a longer time step. A time filter is used to remove the growth of $2\Delta t$ noise, following Asselin (1972). Standard second-order centered differencing is done in space.

3. Model initialization

The two-dimensional west–east domain cross section is perpendicular to the meridionally oriented front. The model domain is periodic in the zonal direction with the length of the domain determined by the wavelength of the most unstable Eady wave perturbation. To isolate the mountain from the effects of the horizontal boundary conditions, the model domain is expanded to accommodate multiple Eady waves.

Comparison of simulations with various domain sizes in which there are multiple Eady waves (one, two, three, and four) without mountains (not shown) reveals that the evolution is not dependent on domain size. When terrain is included, a domain size of two or more Eady wavelengths provide very similar results near the mountain. The three-Eady wave domain is chosen as it sufficiently isolates the mountain from the periodic boundaries. A mountain is placed such that it interacts only with the central Eady wave. For our control simulation the three-Eady wave domain yields a total domain width of 10 520 km and 600 horizontal grid points, yielding a horizontal grid spacing of 17.5 km. Fourteen levels are used in the vertical with $\sigma = 0.1$ except in the lowest four layers where closer spacing is used.

Two-dimensional, steady, rotating, stably stratified flow over a mountain barrier with a rigid lid yields a net deflection of the flow to the right when looking downstream (Merkine 1975; Blumen 1988). The permanent turning of the flow represents the deflection induced by the mountain anticyclone. Merkine (1975) and Bannon (1991) show that for Boussinesq flow over a mountain barrier and an infinite lid the permanent turning is nonexistent. For our simulations with a flexible lid some permanent turning might be expected.

Unfortunately, there is as yet no analytically correct way to initialize nonlinear flow over mesoscale topography. The impulsive mountain initialization is simple and is widely used in the literature. For the impulsive initialization, the model atmosphere is adjusted by removing part of the atmosphere and replacing that section with terrain. As a result, the isentropes initially intersect the terrain. For adiabatic flow, isentropes intersecting the ground will always do so (Smith 1979). Advection of the isentropes along the surface by the low-level wind results in the generation of a shed vortex (Smith 1979, his Fig. 26). The development of the shed vortex does not influence the interaction of the front with the mountain provided it has moved well downstream before the front reaches the windward slope. D95 describe other methods of initialization used during this study. While the details varied slightly between the methods, the results are essentially the same for all methods.

The model is initialized with the analytical semigeostrophic solution to the Eady problem at 50 h following HB72 and Keyser (1981). Note that the baroclinic wave used here is slightly weaker than that used in Keyser (1981), allowing for a longer period of integration before frontal collapse. The model is taken to be on an f plane at 43°N. For the control simulation the maximum surface cyclonic relative vorticity of the Eady wave is positioned 2750 km upstream of the mountain top and allowed to propagate eastward. The initial placement of the front allows sufficient time for the mountain circulation to develop before the front reaches the windward slope. To ensure that the front is positioned well downstream of the mountain before frontal collapse, the Eady wave is embedded in a uniform zonal wind given by a constant C (Table 1). The height and width of the terrain for the control simulation are given in Table 1. Results from several different simulations are presented below. Table 2 provides a summary of the

TABLE 2. List of all simulations performed in this study. Mountain height (in km), mountain width (in km), Froude number, and Rossby number for each simulation are provided. Here U is the mean wind upstream of the mountain, L is the mountain half-width, N is the static stability, and H is the mountain height.

Name	Description	Height (H)	Half-width (L)	Fr = U/NH	Ro = U/fL
Control	Front with mountain	1.0 km	500 km	0.67	0.15
Front	Front only	0 km	0 km	—	0.00
Mountain	Mountain only	1.0 km	500 km	0.67	0.15
H1500	Tall mountain	1.5 km	500 km	0.44	0.15
H500	Low mountain	0.5 km	500 km	1.34	0.15
L250	Front with narrow mountain	1.0 km	250 km	0.67	0.40
L1000	Front with wide mountain	1.0 km	1000 km	0.67	0.01
β30	Weak front	1.0 km	500 km	0.67	0.15
β70	Strong front	1.0 km	500 km	0.67	0.15

mountain and flow characteristics for each case. Note the values of Fr and Ro are obtained from the basic-state surface wind and stability profile. Inclusion of the Eady wave perturbation in these calculations does not significantly change these values.

4. Results

a. Mountain-only simulation

For the mountain-only simulation, the model is initialized with the Eady basic state and a single mountain. The evolution of the surface (lowest σ layer) relative vorticity (hereafter surface vorticity) and horizontal divergence are shown in Fig. 1. The first vorticity center on the lee slope, developing shortly after the model integration begins, is the shed vortex. As noted by Smith (1979), the shed vortex is due solely to the impulsive mountain initialization. After the shed vortex moves downstream, a band of cyclonic relative vorticity develops and remains stationary along the lee slope. This band of vorticity, called the lee trough, results from the generation of inertia-gravity waves. Note the asymmetric mountain circulation is due to upward propagating inertia-gravity waves, which are not present in quasigeostrophic or semigeostrophic models.

In addition to the shed vortex and stationary mountain waves, there is a relative vorticity center that develops near the base of the lee slope (x = 500 km) just before 30 h. This vorticity center forms in association with the establishment of the lee trough. Before reaching a steady state, vorticity in the lee trough reaches a maximum shortly after it develops (Fig. 1a). Warm advection ahead

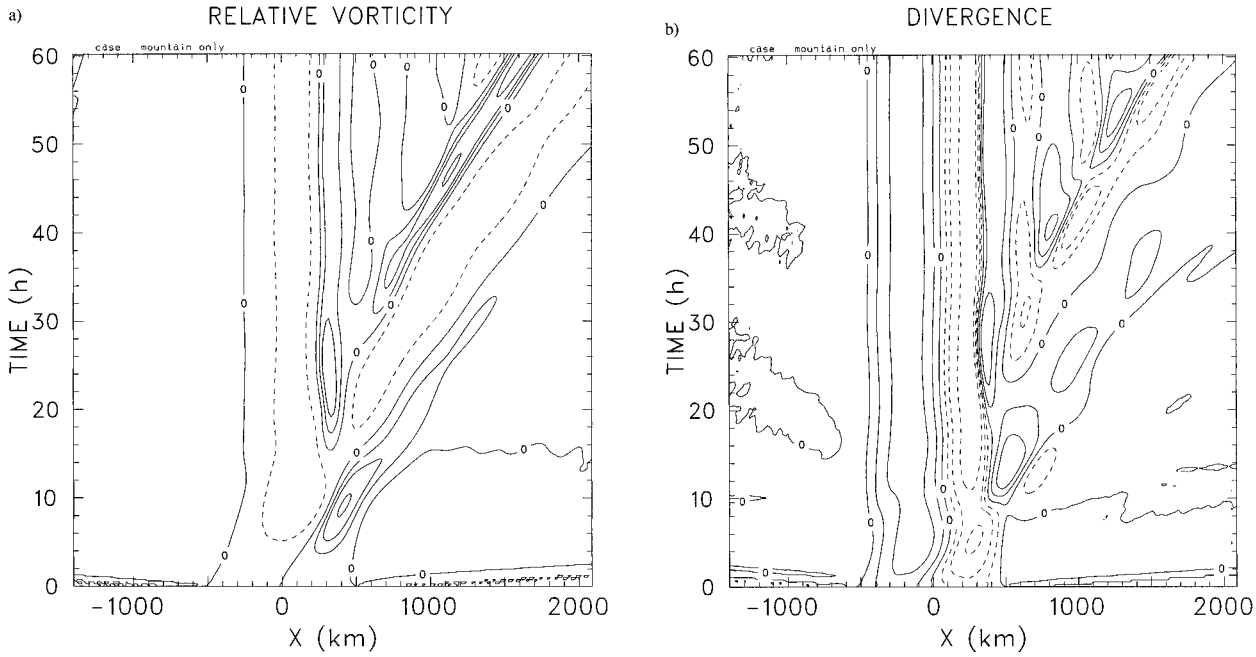

FIG. 1. Time variation of the surface (lowest σ level) (a) relative vorticity and (b) divergence for the mountain-only simulation. (a) Relative vorticity scaled by 1.0×10^{-4} and (b) divergence scaled by 1.0×10^{-5}. Negative values are dashed (a). Values of -0.25, 0.0, 0.25, 0.50, and 1.00 are contoured. (b) Values of -4.0, -2.0, -1.0, 0.0, and 1.0 are contoured.

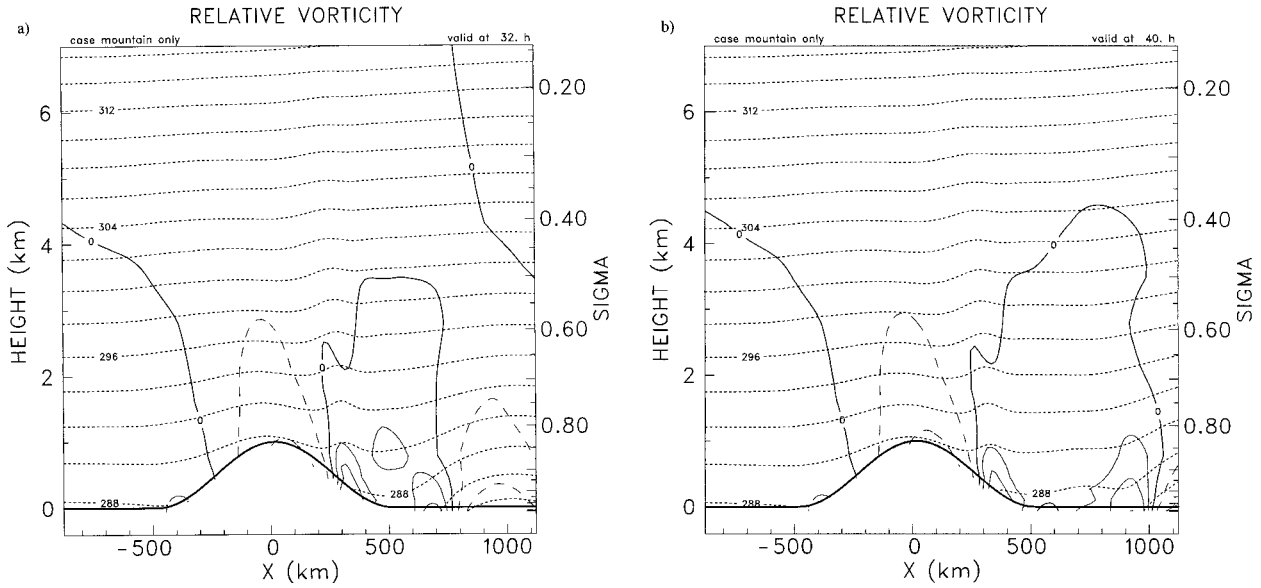

FIG. 2. Vertical cross sections of relative vorticity and potential temperature (small dashed lines) at (a) 32 h and (b) 40 h for the mountain-only case. Relative vorticity scaled by 1.0×10^{-4}. Contour interval for potential temperature is 2 K. Contour interval for relative vorticity as in Fig. 1a with -0.125 and 0.125 contours added.

of the lee trough acts to lower surface pressures near the base of the lee slope, leading to the generation of negative ageostrophic vorticity, horizontal convergence (Fig. 1b), and cyclonic relative vorticity (equivalently, with uniform PV in the interior, warm advection ahead of the lee trough lowers the stability near the base of the lee slope leading to the spinup of relative vorticity there). This vorticity center strengthens as it propagates downstream. Vertical cross sections of relative vorticity at 32 h (Fig. 2a) and 40 h (Fig. 2b) show the increasing strength and vertical extent of this feature. The depth and strength of this feature continue to increase as it moves downstream (not shown).

Since this basic state is baroclinically unstable it appears that the mountain provided a disturbance that could grow on this basic state. This vorticity feature is not observed in barotropic simulations and is present regardless of how the baroclinic simulation was initialized (D95). Although it is not discussed, a similar development is observed in K92 (their Fig. 14b). The strength of this vorticity feature depends on mountain size while its location is approximately constant (not shown). Strongest vorticity is produced by flow over tall or narrow mountains. Further investigation is necessary to understand the development of this vorticity feature.

Unlike Bannon and Zehnder (1989), who find a steady state for semigeostrophic baroclinic flow over the ridge, no steady state is achieved during this simulation. With periodic boundary conditions, both the shed vortex and baroclinically generated vortex will remain in the model domain for all time, preventing the establishment of a steady state.

b. Front–mountain simulation

For the control simulation, the model is initialized with three Eady waves across the domain. Only the center Eady wave interacts directly with the terrain. The evolution of the surface vorticity, the cross-front thermal gradient (hereafter thermal gradient), and divergence for the control simulation is shown in Fig. 3. For reference, the evolution of the surface vorticity and the thermal gradient for the front only case are shown in Fig. 4.

The surface front, as defined by the surface vorticity maximum, reaches the foot of the windward slope by 24 h (Fig. 3a). The approach of the front has also led to an intensification of the lee trough vorticity. Although a similar strengthening of the lee trough is observed in the mountain-only case (Fig. 1a), the rate of intensification is larger for the control simulation (Fig. 3a). The increased intensification of the lee trough was produced by: (a) increased cross-mountain flow associated with the approaching front (not shown) and (b) the larger-scale convergence associated with the Eady wave phasing with the lee trough.

The surface front is increasingly slowed as it moves along the windward slope (Figs. 3a, 3b). Further evidence is shown in Fig. 5, which shows vertical cross sections of relative vorticity and potential temperature. While the surface vorticity maximum is slow to move along the windward slope, propagation of the upper-level wave is not affected by the terrain. This is reflected by the frontal slope, as measured by the vertical distribution of relative vorticity, becoming increasingly vertical in time (Figs. 5a–c). Weakening of the frontal vorticity and thermal gradient is observed along the

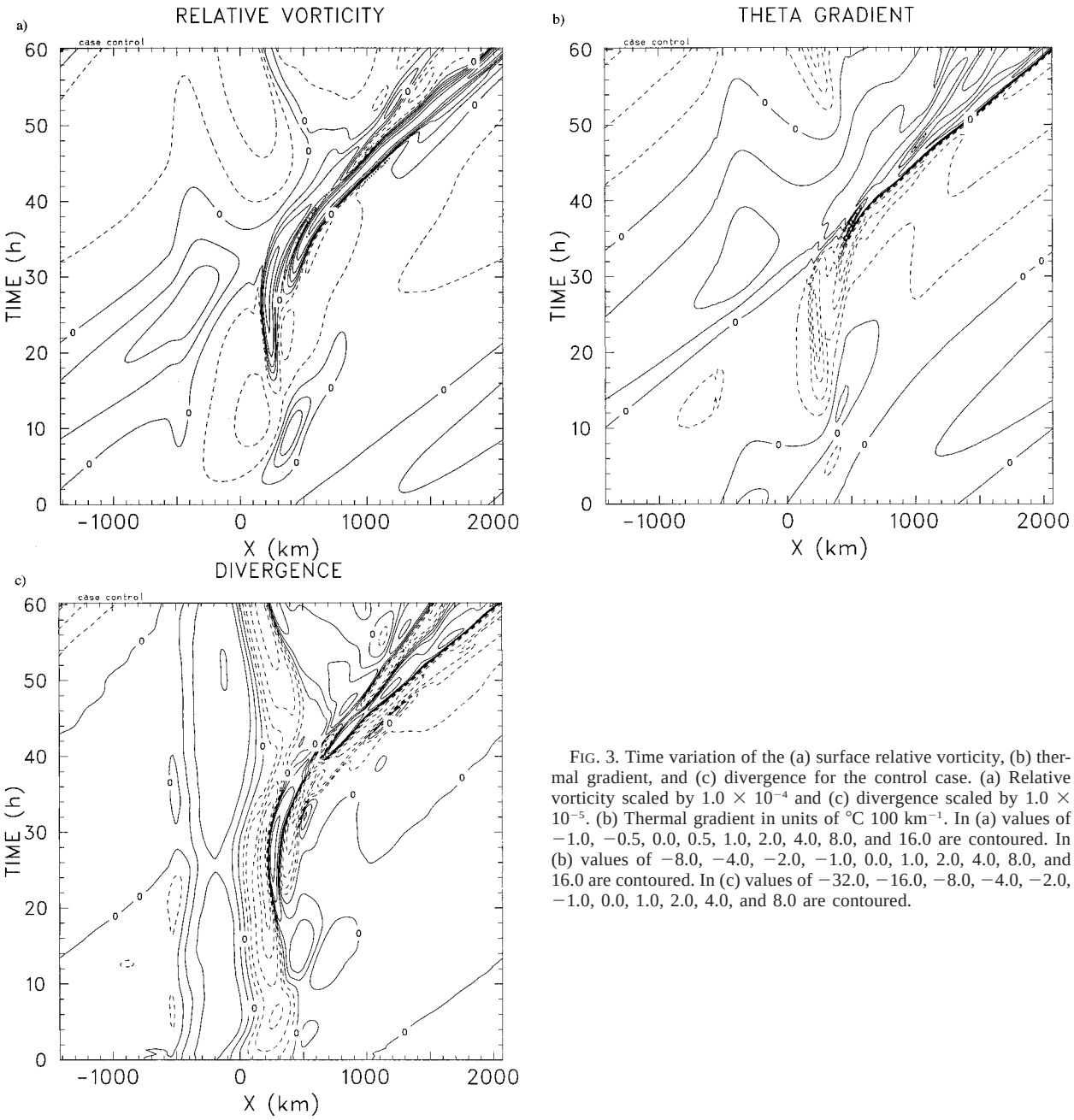

FIG. 3. Time variation of the (a) surface relative vorticity, (b) thermal gradient, and (c) divergence for the control case. (a) Relative vorticity scaled by 1.0×10^{-4} and (c) divergence scaled by 1.0×10^{-5}. (b) Thermal gradient in units of °C 100 km^{-1}. In (a) values of -1.0, -0.5, 0.0, 0.5, 1.0, 2.0, 4.0, 8.0, and 16.0 are contoured. In (b) values of -8.0, -4.0, -2.0, -1.0, 0.0, 1.0, 2.0, 4.0, 8.0, and 16.0 are contoured. In (c) values of -32.0, -16.0, -8.0, -4.0, -2.0, -1.0, 0.0, 1.0, 2.0, 4.0, and 8.0 are contoured.

windward slope. It is difficult, however, to separate vorticity weakening from masking by the mountain anticyclone.

Beginning shortly after 28 h, a new surface vorticity maximum (hereafter secondary trough) develops near the base of the lee slope at $x = 450$ km (Figs. 3a, 5b, 5c). A similar vorticity development occurs slightly later in the mountain-only simulation described previously (Fig. 1a). Upper-level PV advection associated with the approaching front over the secondary trough further encourages cyclonic vorticity growth near the base of the lee slope. This results in a stronger secondary trough than was observed in the mountain-only case (Figs. 1a, 3a). Potential vorticity advection associated with an upper-level trough has been suggested by Mattocks and Bleck (1986) as a possible trigger for lee cyclogenesis. Upper-level PV advection is not strongly affected by the mountain (not shown).

To further illustrate the effect of the upper-level PV advection Fig. 6 shows vertical motion (in pressure coordinates) at 32 h for the (a) front-only, (b) mountain-only, and (c) control simulations. Ascent and descent

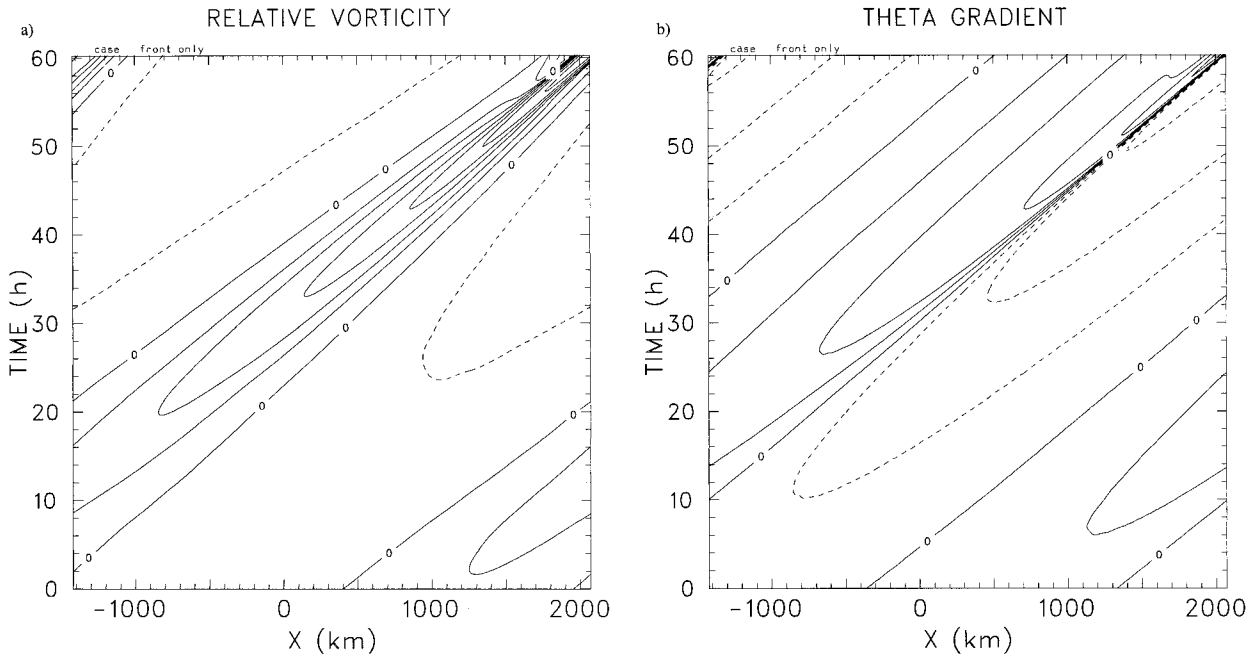

FIG. 4. Time variation of the (a) relative vorticity and (b) thermal gradient for the front-only case. Scaling as in Fig. 3. (a) Values of −0.5, 0.0, 0.5, 1.0, 2.0, 4.0, 8.0, and 16.0 are contoured. (b) Values of −1.0, −0.5, 0.0, 1.0, 2.0, 4.0, 8.0, and 16.0 are contoured.

on the lee side of the mountain is much larger in the control simulation than in the mountain-only simulation. This difference is due, in part, to the forcing of upward motion in the region by the approaching upper-level PV anomaly associated with the Eady wave. The vertical velocity in the control is larger than the sum of the mountain-only and front-only vertical velocities, showing the nonlinear aspects of the interaction.

By 34 h (Figs. 3a and 5d), rapid intensification of the secondary trough near the base of the lee slope occurs as the upper-level wave moves into phase and couples with the secondary trough near the foot of the lee slope (Figs. 3a, 5d, 5e). The secondary trough marks the position of the new surface vorticity front. The original surface vorticity front remains trapped along the windward slope but has been significantly weakened by the mountain circulation.

The evidence presented here indicates that the frontal propagation across the ridge is a discontinuous process. This is in agreement with Keuler et al. (1992), who also showed a discontinuous propagation across the terrain. The mountain circulation disrupts the front, acting to separate the surface front from its associated upper-level wave. The original surface vorticity front stalls along the windward slope of the mountain and a new vorticity front (secondary trough) develops at the base of the lee slope, independent of the original surface vorticity front. The upper-level wave then couples with this secondary trough and moves downstream.

By disrupting the approaching frontal circulation, it appears that the mountain acts to briefly decouple the surface thermal and vorticity fronts. Separation of the thermal front from the vorticity (wind shift) front is a result of the blocking of the original surface vorticity and cold air along the windward slope and development of a new surface vorticity front at the base of the lee slope, approximately 400 km ahead of the leading edge of cold air (Figs. 3a, 3b). The separation is reduced once the cold air passes over the ridge.

A comparison of front only to the control case shows that after 60 h, there is no difference in the positions of the surface vorticity and thermal fronts. In addition, there is little difference in the strength of the relative vorticity after 60 h (Figs. 3a and 4a). Conversely, the surface thermal front is stronger after the interaction with terrain, supporting the findings of K92 (Figs. 3b and 4b). This contradicts the results of W92, who showed no net change in frontal strength downstream of the mountain. The difference is due to the asymmetric mountain circulation. The asymmetric nature of the frontogenesis across the ridge will be made clearer in the following section.

To identify the effects of the mountain on the surface frontal vorticity structure, we subtract the mountain-only simulation from the control simulation (Fig. 7). The remaining fields contain the front-only solution as well as the nonlinearities that result from the interaction with terrain. If the result of the interaction was purely due to superposition, this subtraction would yield frontal development identical to Fig. 4a. The difference field shows the stronger lee trough present in the control simulation, as noted previously. The frontal circulations

are significantly disrupted by the interaction. Comparison with Fig. 4a shows that after the interaction, the surface frontal vorticity is stronger and has a decreased cross-front scale compared to the no-mountain case.

c. Budget calculations

The two-dimensional vorticity and frontogenesis equations at the surface are

$$\frac{d}{dt}\left(\frac{\partial v}{\partial x}\right) = -\left(\frac{\partial v}{\partial x} + f\right)\frac{\partial}{\partial x}u_{ag} + \frac{\partial}{\partial x}\left(\frac{\partial v}{\partial t_{diff}}\right), \quad (3)$$

$$\frac{d}{dt}\left(\frac{\partial \theta}{\partial x}\right) = -\left[\frac{\partial u}{\partial x}\frac{\partial \theta}{\partial x} + \frac{\partial v}{\partial x}\frac{\partial \theta}{\partial y} - \frac{\partial}{\partial x}\left(\frac{\partial \theta}{\partial t_{diff}}\right)\right], \quad (4)$$

respectively. Changes in vorticity (3) are due to vertical stretching and diffusion. Frontogenesis (4) is controlled by stretching deformation (horizontal convergence), shearing deformation (relative vorticity in 2D simulations), and diffusion. In this form, negative values of $(d/dt)(\partial\theta/\partial x)$ may reflect both cold frontolysis and warm frontogenesis. This distinction will be made clear in the text.

Vorticity generation due to horizontal convergence is shown in Fig. 8. Weak anticyclonic vorticity production (negative vorticity tendency) is seen on the windward slope associated with the weak mountain-forced divergence. Two distinct bands of positive vorticity generation are present on the lee slope. The first is associated with the rapid spin up of the lee trough. The second, located near the base of the lee slope, is associated with the rapid development of convergence there, discussed previously (Fig. 3c). The growth of convergence in the control simulation is further encouraged by upper-level PV advection associated with the approaching front. The rapid growth of convergence (not shown) leads to rapid vorticity growth at the base of the lee slope (Fig. 8), supporting the development of the new surface vorticity front (Fig. 3a)

Frontogenesis due to stretching deformation (divergence in the 2D simulations) is presented in Fig. 9a. Divergence acting on the cold frontal thermal gradient (Fig. 3b) produces weak frontolysis along the windward slope after 25 h. Two intense bands of negative thermal gradient develop on the lee slope as the surface front approaches and moves along the windward slope. These frontogenesis bands are a result of the lee-slope convergence acting on the negative thermal gradient of the Eady wave to produce warm fronts (Figs. 3b,c). Away from the mountain, the warm frontogenesis weakens due to an unphasing of the convergence and warm frontal gradient. After 40 h, a narrow band of cold frontogenesis develops as the convergence becomes slightly in phase with positive thermal gradient (Figs. 3b,c).

Since the meridional temperature gradient is always negative, cold frontogenesis due to shearing deformation will occur wherever the relative vorticity is cyclonic (Figs. 3a, 3b, 9b). Frontogenesis due to this term gradually weakens as the front moves up the windward slope. The rapid growth of the secondary trough produces a strong region of frontogenetical forcing. Since the new surface vorticity front is initially associated with a warm frontal temperature gradient (Figs. 3a,b), shearing deformation will continually act to weaken the warm front and generate a cold frontal gradient.

The total frontogenesis (Fig. 9c) shows weak frontogenesis along the windward slope due to shearing deformation up to 30 h. Along the lee slope, frontogenesis is oriented in a banded pattern, a result of the out of phase relationship between the shearing deformation (vorticity) and stretching deformation (convergence) between 20 and 35 h (Fig. 13c). Orlanski and Ross (1984) suggest that the out of phase relationship between shearing and stretching deformation acts as a governor on frontogenesis. Frontogenesis continues to be weak along and downstream of the lee slope. After 40 h however, both shearing and stretching deformation terms contribute positively to cold frontogenesis. This is the time at which the surface thermal gradient in the control simulation becomes stronger than in the front-only simulation (Figs. 3b, 4b). A comparison of the control (Fig. 9c) and front only (not shown) simulations show that the total frontogenesis is twice as strong at 40 h in the control case.

5. Sensitivity studies

Previous results (Davies 1984; Schumann 1987; Haderlein 1989; Egger 1992; Gross 1994) note that the characteristic behavior of the front–mountain interaction can be determined by the Froude ($\mathrm{Fr} = U/NH$) and Rossby ($\mathrm{Ro} = U/fL$) numbers, which, for fixed N and f, are measures of the nondimensional mountain height and width. The value $\mathrm{Ro\,Fr^{-1}}$ is a measure of nondimensional mountain slope. There is a distinct relationship between the size of Fr and the amount of retardation. Fronts were blocked when mountains were tall (small Fr) or when the mountain slopes were steep (large $\mathrm{Ro\,Fr^{-1}}$). Schumacher et al. (1996) note that, based on Fr, a majority of the fronts in their study would not have been able to cross the Appalachians. Gross (1994) and Schumacher et al. (1996) suggested the importance of frontal strength on frontal propagation. This section considers the sensitivity of the frontal propagation characteristics to different frontal strengths and topographic parameters. A brief description of the cases is given in Table 2. For brevity, this section will focus on the evolution of the low-level vorticity field.

a. Mountain size

Figure 10 shows the surface vorticity evolution for cases H1500 and H500 (see Table 2). For H1500 (Fig. 10a), the large $\mathrm{Ro\,Fr^{-1}}$ and Fr much less than 1 indicates strong low-level blocking will occur along the windward slope. For reference, Pierrehumbert and Wyman (1985) noted that for Fr values less than 1.33, upstream flow

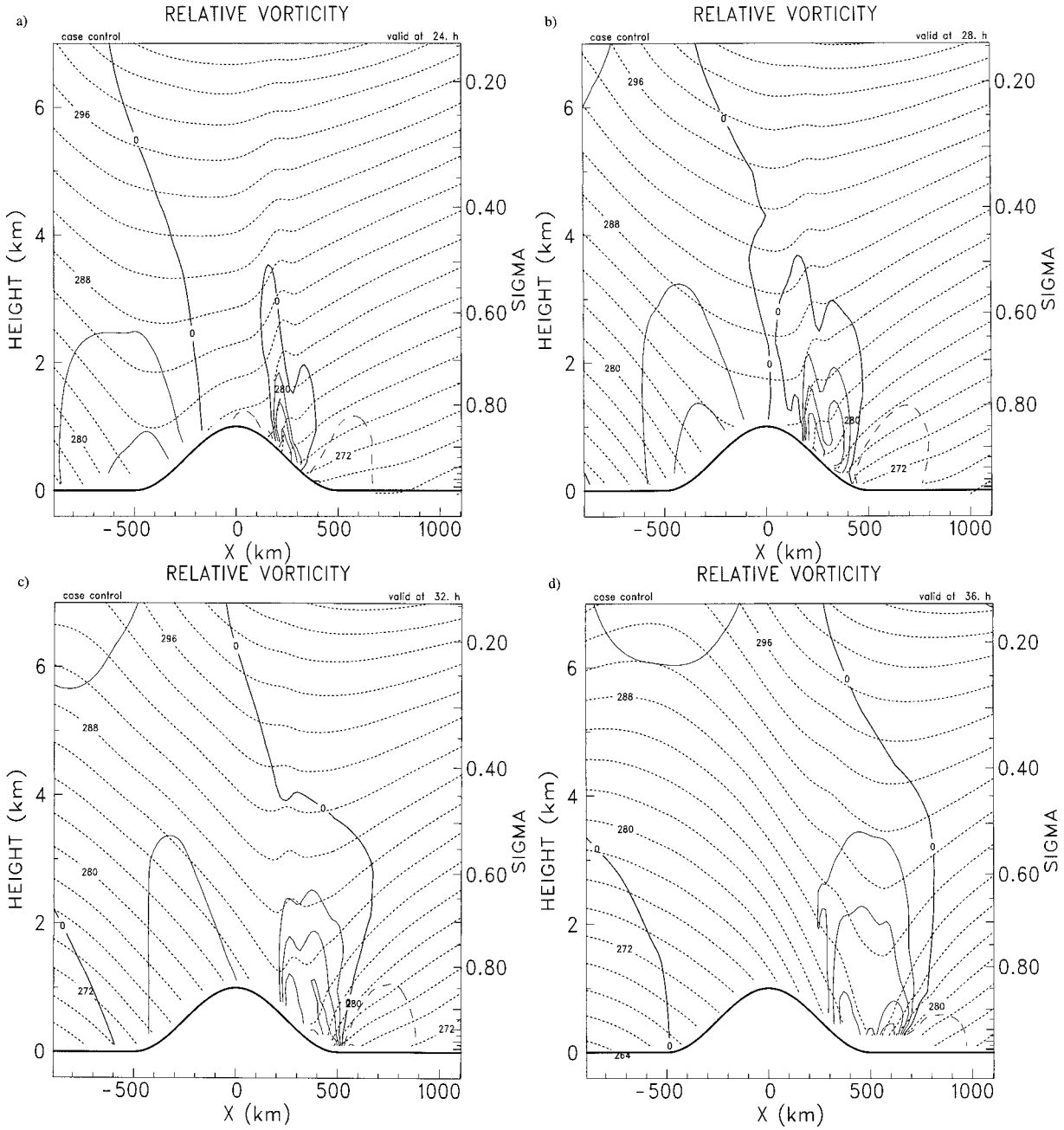

FIG. 5. Vertical cross sections of relative vorticity and potential temperature (small dashed lines) at t = (a) 24 h, (b) 28 h, (c) 32 h, (d) 36 h, and (e) 40 h. Contour interval of 2 K for potential temperature. Scaling and contour interval for relative vorticity as in Fig. 3a.

blocking is expected. As expected, the approaching surface front is blocked along the windward slope (Fig. 10a), causing the frontal slope to become increasingly steeper, allowing the upper-level wave to eventually decouple from the low-level wave (not shown). Similar to the control simulation, the approaching front has produced a rapid strengthening of the lee trough and a secondary trough at the base of the lee slope between 20 and 30 h (Fig. 10a). The secondary trough rapidly strengthens once the upper-level wave moves across the ridge (not shown). This new surface vorticity center becomes the new surface front. The propagation of the vorticity front for tall mountains is discontinuous.

Figure 10b shows only weak low-level blocking is observed along the windward slope in case H500 (small $\mathrm{Ro}\,\mathrm{Fr}^{-1}$ and Fr greater than 1). The lower mountain produces weaker downslope flow and a weaker lee trough compared to the control. The reduced low-level

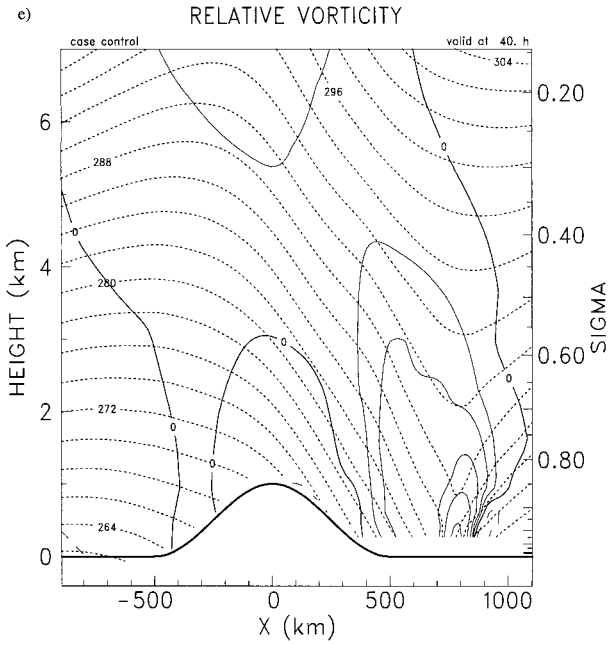

FIG. 5. (*Continued*)

blocking suggest that the upper- and lower-level waves will remain coupled. Once the surface front reaches the top of the ridge, it is accelerated down the lee slope by the cross-mountain flow. A weak secondary trough is suggested at the base of the lee slope by 30 h (Fig. 10b). This secondary trough is quickly incorporated into the surface front. Frontal propagation across the ridge is continuous for low mountains.

The effects of varying mountain width are shown in Fig. 11. For the narrow mountain case, L250, the Ro is around 0.4 indicating the increased importance of mesoscale dynamics. The value of $\mathrm{Ro\,Fr^{-1}}$ in L250 is comparable to that of H1500, suggesting that these cases will exhibit similar features. Frontal blocking and weakening is observed along the windward slope, allowing the upper- and lower-level frontal waves to decouple. As in the previous cases, the approach of the front leads to a dramatic strengthening of the lee trough and secondary trough at the base of the lee slope. The secondary trough becomes the dominant surface feature. Once the upper-level couples with the surface vorticity, the new front moves downstream. For large Ro, the propagation of the vorticity front is discontinuous across the ridge.

For wide mountains (L1000, Fig. 11b) the small Ro number indicates that the flow is nearly geostrophic and that little blocking will occur. The value of $\mathrm{Ro\,Fr^{-1}}$ in case L1000 is similar to case H500, suggesting that L1000 and H500 will appear similar. The reduced blocking indicates that the upper- and lower-level waves will remain coupled as the front passes over the mountain. Once near the top of the mountain, the front is accelerated across the ridge. Only a weak lee trough is observed during this case. Once the front moves to the lee slope, the surface vorticity strengthens rapidly. When the Ro is small, the propagation of the vorticity front over the ridge is continuous.

Consistent with the results from the control simulation (Fig. 3), there is little difference in the final position of surface vorticity between cases H1500, H500, L1000, L250, and front only well downstream of the mountain (Figs. 3a, 10, 11). In terms of frontal strength, the thermal gradient is stronger after the interaction for all simulations (not shown) while there is no net change in the vorticity strength (Fig. 3a, 10, and 11). This is a direct result of the mountain focusing the frontogenetical forcing at the base of the lee slope, whereas the vorticity growth is dictated by the larger scale Early wave. In all cases, the front reaches the position $x = 500$ km sooner, stronger, and with a decreased cross-front scale than if no mountain was present.

These results suggest that one of the most important parameters in diagnosing frontal blocking is the nondimensional mountain height $\mathrm{Ro\,Fr^{-1}}$. When $\mathrm{Ro\,Fr^{-1}}$ is large (tall or narrow mountains), the surface front is strongly blocked along the windward slope. Frontal propagation is said to be discontinuous. When $\mathrm{Ro\,Fr^{-1}}$ is small (low or wide mountains), the windward blocking is greatly reduced allowing the surface front to propagate across the mountain.

b. Frontal strength

To determine the importance of frontal strength on frontal propagation, two additional simulations are performed. Initial frontal strengths result from specifying different starting time in the analytical semigeostrophic solution to the Eady problem. The weak front, $\beta 30$, and strong front, $\beta 70$, are obtained by specifying an initial time of 30 h and 70 h, respectively. Note that for these cases, both the terrain and background flow are identical to the control case (see Table 2). The no-mountain solution for these cases is similar to Fig. 2a.

For case $\beta 30$, the weak frontal circulation is expected to be dominated by the mountain circulation. The surface vorticity front in $\beta 30$ is strongly weakened and decelerated along the windward slope (Fig. 12). With the weak vertical frontal circulation and strong low-level blocking, the upper-level wave is more easily decoupled from the lower-level wave than in previous cases (not shown). As in the control, the approach of the front has led to an intensification of the lee trough and secondary vorticity maximum at the base of the lee slope. The new surface front is considerably stronger and has a much smaller cross-front scale compared to the no-mountain case (not shown). Once away from the terrain, the surface front in $\beta 30$ moves somewhat slower than in the absence of terrain so that by 60 h, the new surface front lags behind the no-mountain case by 200 km (cf. Figs. 12 and 3a). This may be a result of the lack of vertical

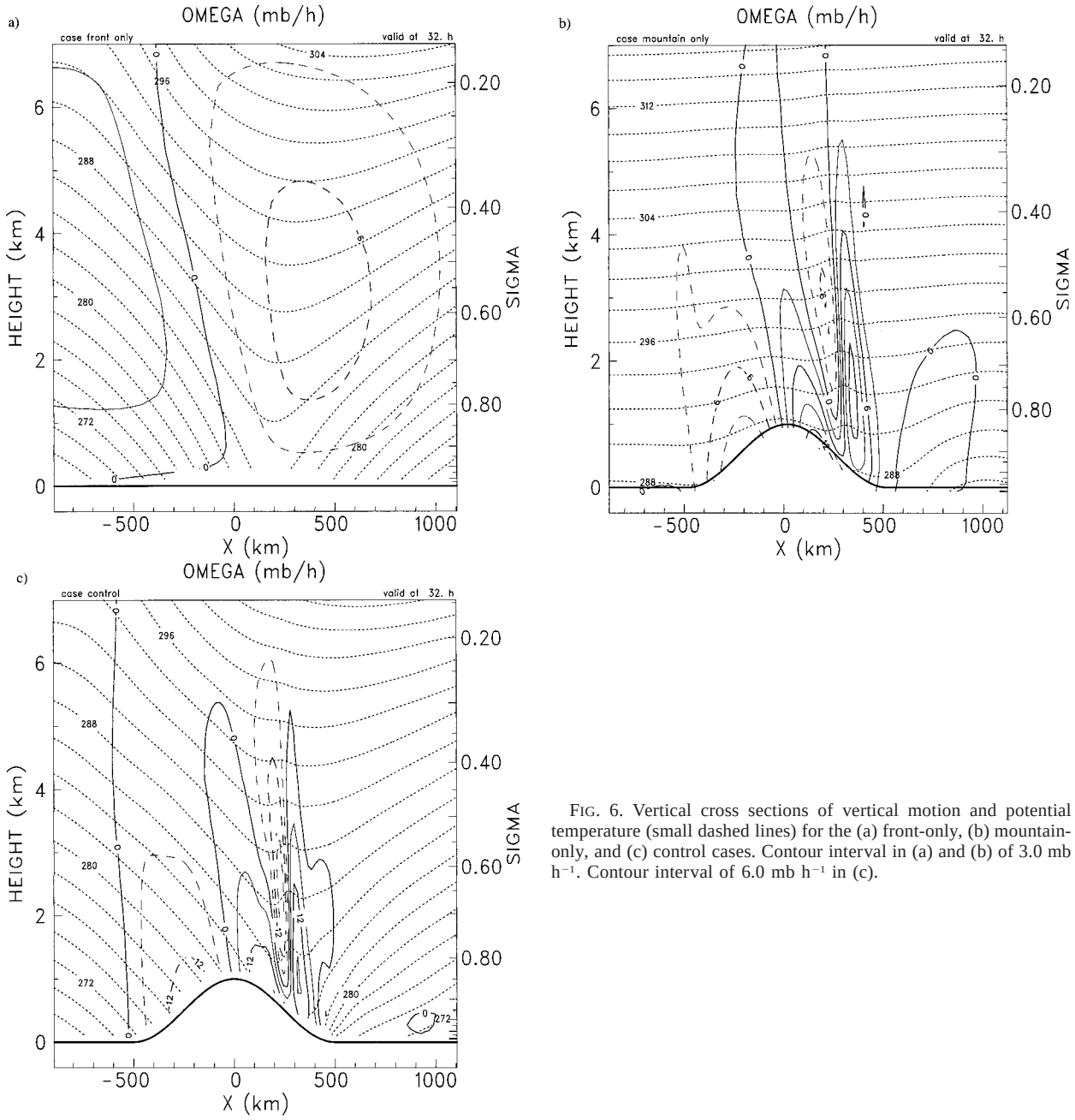

FIG. 6. Vertical cross sections of vertical motion and potential temperature (small dashed lines) for the (a) front-only, (b) mountain-only, and (c) control cases. Contour interval in (a) and (b) of 3.0 mb h^{-1}. Contour interval of 6.0 mb h^{-1} in (c).

coupling between the weaker upper- and lower-level fronts.

The evolution is markedly different when a strong front is considered. Since the front exhibits a vigorous vertical circulation (not shown), it is expected that the mountain circulation will exert a lesser influence on frontal propagation. Figure 13 shows a slight retardation of the surface front along the windward slope. The strong tropospheric deep frontal circulation associated with $\beta 70$ ensures that the lower-level wave remains coupled with the upper-level wave. The surface vorticity is noticeably weaker as the front approaches the top of the mountain. Since the surface front is not blocked by the terrain, the lee trough does not have time to develop and is absorbed into the passing front. For case $\beta 70$, the front reaches the position of $x = 500$ km approximately 1 h sooner and slightly stronger than its no-mountain counterpart (not shown). By 60 h the position of the surface vorticity is the same for the no-mountain and mountain cases.

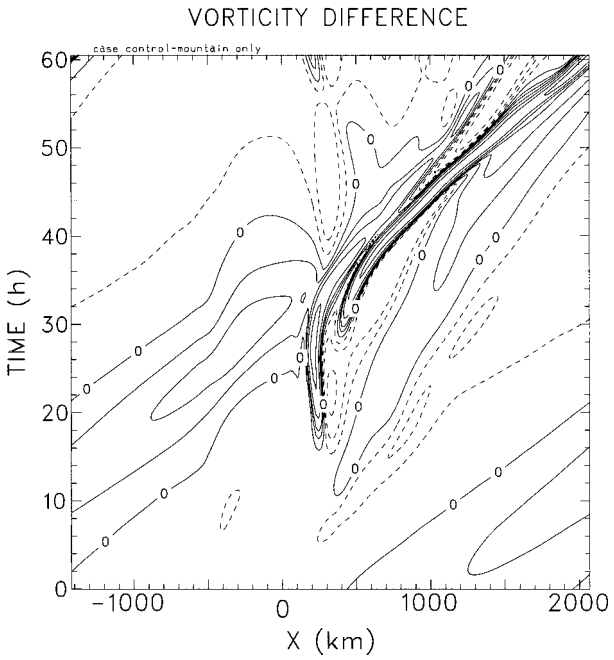

FIG. 7. Time variation of the surface vorticity difference between the control and the front-only case. Scaling and contour interval as in Fig. 3a.

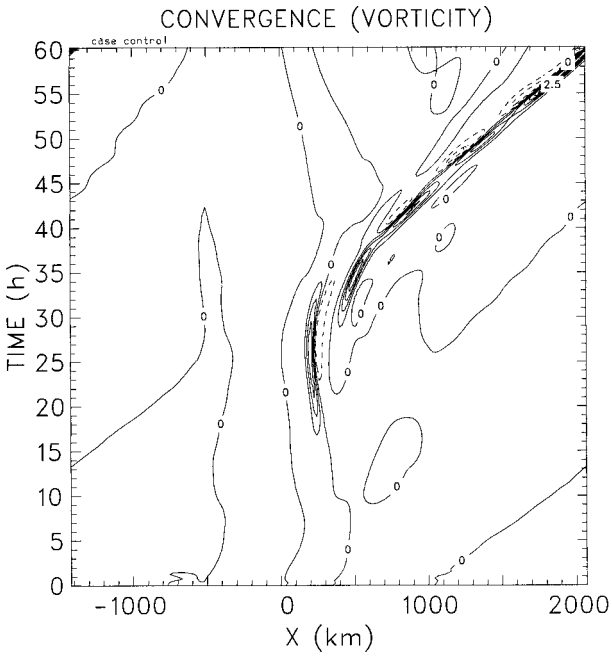

FIG. 8. Time variation of the surface vorticity tendency due to convergence for the control case. Units of $1.0 \times 10^{-4}\ s^{-1}\ h^{-1}$. Contour interval of 0.5.

6. Conclusions

A two-dimensional primitive equation hydrostatic model is used to investigate the problem of frontal interaction with mesoscale topography. Frontogenesis is a result of the shearing deformation mechanism following HB72. The analytical solution to the semigeostrophic Eady wave is used to initialize the model following Keyser and Anthes (1982). This developing Eady wave includes the effects of an upper-level PV anomaly and a baroclinic basic state. Particular attention is given to determining the frontal propagation across the ridge and what the net effect of the mountain on frontal characteristics is well downstream of the mountain.

The propagation of the Eady wave across the terrain is summarized schematically in Fig. 14. In all simulations, the approaching front was slowed and weakened by the mountain circulation along the windward slope (Figs. 14a,b). The degree of the blocking along the windward slope is dependent on the nondimensional height and width of the mountain. If the low-level blocking is significant, the frontal slope steepens and the upper-level PV anomaly associated with the growing front is able to separate from the surface front. This upper-level wave propagates across the domain unaffected by the terrain. The approach of the upper-level wave leads to a strengthening of the lee trough and secondary lee trough due to the superposition and interaction of the mountain and Eady wave convergence (Figs. 14b,c).

As the upper-level wave passes across the mountain it is able to couple with the newly generated secondary trough at the base of the lee slope resulting in the establishment of a new front (Fig. 14d). The new front then propagates downstream away from the mountain. Thus, the frontal propagation is discontinuous across the ridge. The original surface front is eventually eroded along the windward slope.

The propagation across the ridge is more continuous for mountains with shallow slopes. The mountain is unable to significantly block the approaching surface front, allowing the upper- and lower-level waves to remain coupled. The lee trough is present in these simulations, but is weaker than that observed in the control simulation. Since the mountain is unable to significantly slow the surface front, the lee trough has less time to become organized. Downstream of the mountain, the surface front is a combination of the original surface front and the weak secondary trough generated at the base of the mountain.

The propagation across the ridge is discontinuous for weak fronts. Weak fronts have frontal circulations that can be easily disrupted by the terrain. The mountain is able to block the approaching surface front allowing the upper-level wave to decouple from the blocked surface front. Strong fronts, with a more intense upper-level PV anomaly and ageostrophic circulations, are not significantly affected by the terrain. Results show that there is only a slight retardation and weakening along the windward slope The lack of appreciable blocking along the windward slope and the strong frontal circulation allows the front to remain intact across the ridge. As a

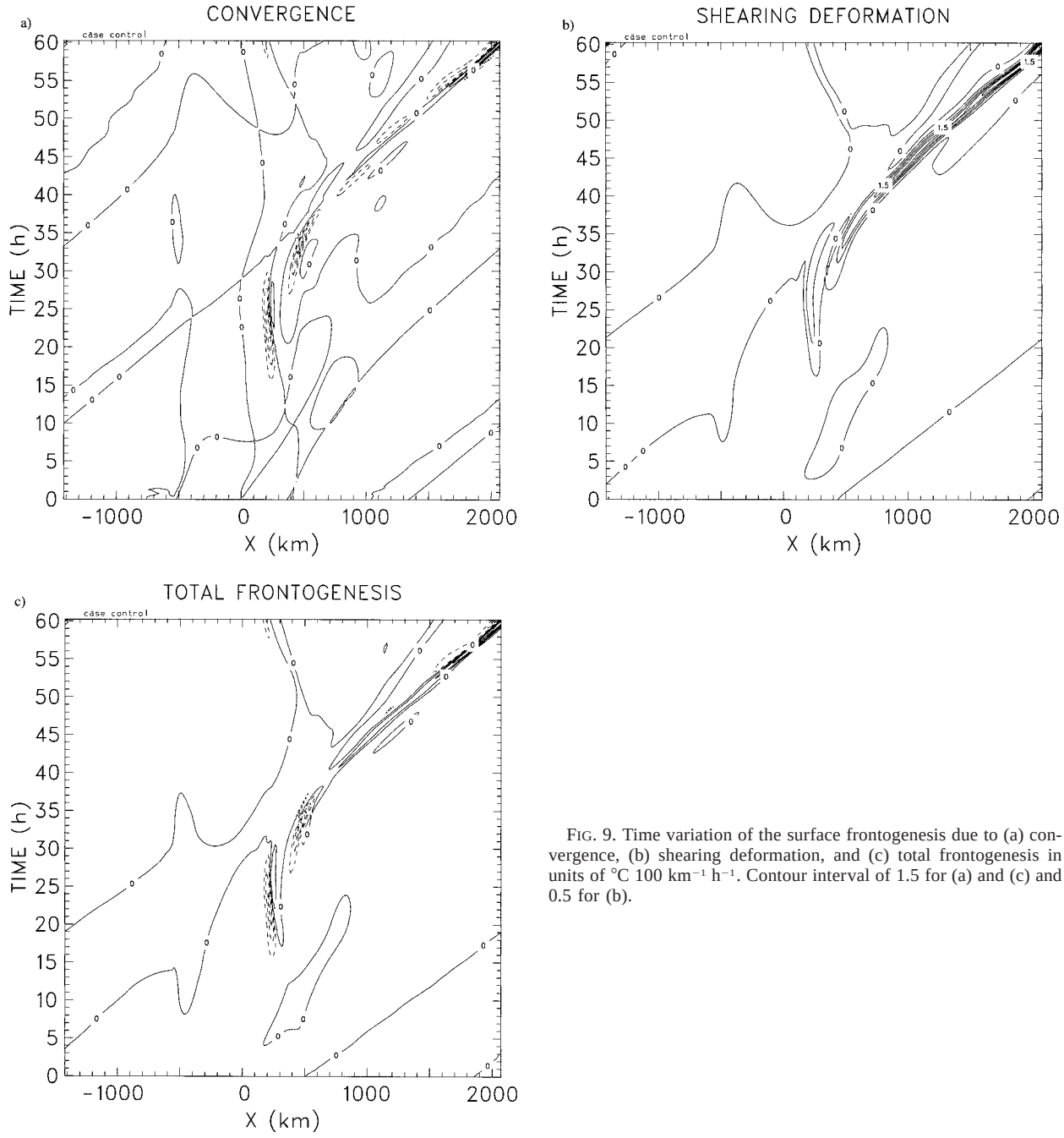

FIG. 9. Time variation of the surface frontogenesis due to (a) convergence, (b) shearing deformation, and (c) total frontogenesis in units of °C 100 km^{-1} h^{-1}. Contour interval of 1.5 for (a) and (c) and 0.5 for (b).

result, the strong front is able to pass across the terrain with little interruption. These results support the observational results of Schumacher et al. (1996), who noted the importance of the strength of the upper-level PV anomaly.

Comparison of the surface vorticity for the front-only and front–mountain cases shows that the new surface front is stronger and has a decreased cross-frontal scale after the mountain interaction. Well downstream of the mountain, however, there is no net position change in either vorticity and cross-front thermal gradient. This suggests that it is the upper-level wave associated with the growing front and not the mountain that controls frontal propagation well downstream of the ridge.

The surface thermal front is stronger well downstream of the mountain in disagreement with the results of W92. This may be explained by the asymmetric nature of the frontogenesis patterns across the terrain forced by the upper-level wave and the inclusion of alongfront temperature advections in this study. In addition, the net

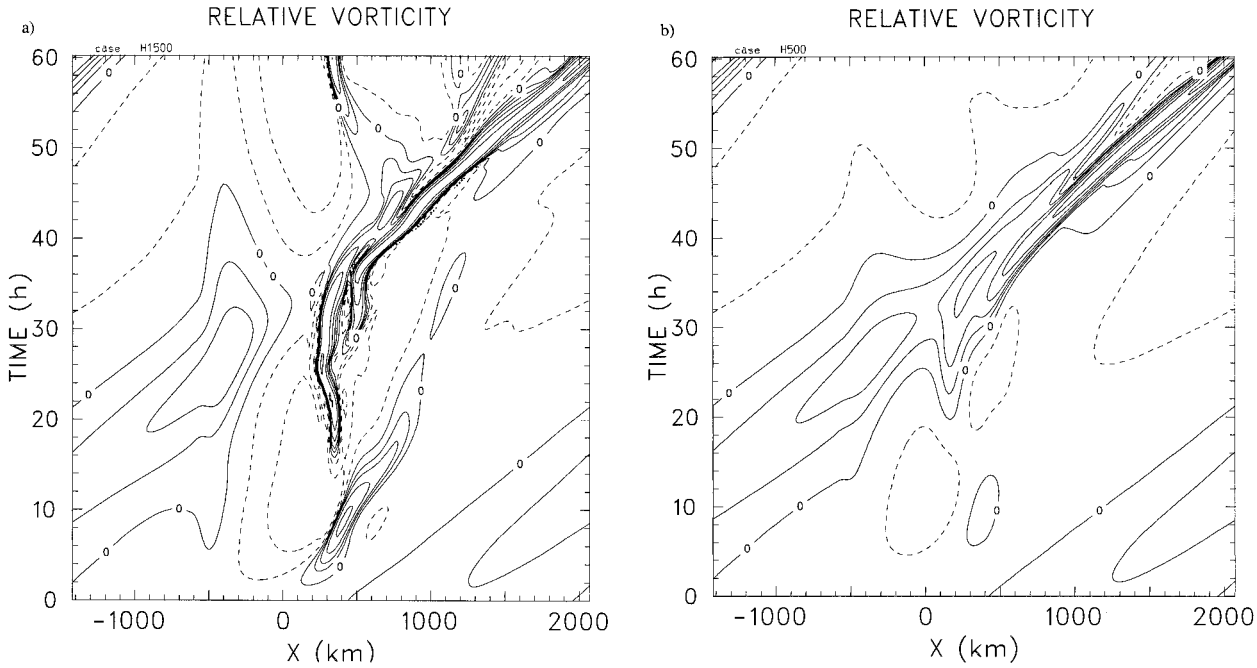

FIG. 10. Time variation of the surface relative vorticity for (a) H1500 and (b) H500. Scaling and contour interval as in Fig. 3a.

effect of the mountain is to separate the vorticity and thermal fronts. Results show that as the front interacts with the terrain, the wind shift can lead the thermal front by several hundred kilometers.

Future work includes adding moisture and boundary layer physics into the model. Inclusion of these parameters may have considerable effect on the mountain circulation and frontal propagation across the mountain.

Acknowledgments. This paper presents results of the first author's master's thesis research at the State University of New York at Albany. This research was supported in part by the National Science Foundation by

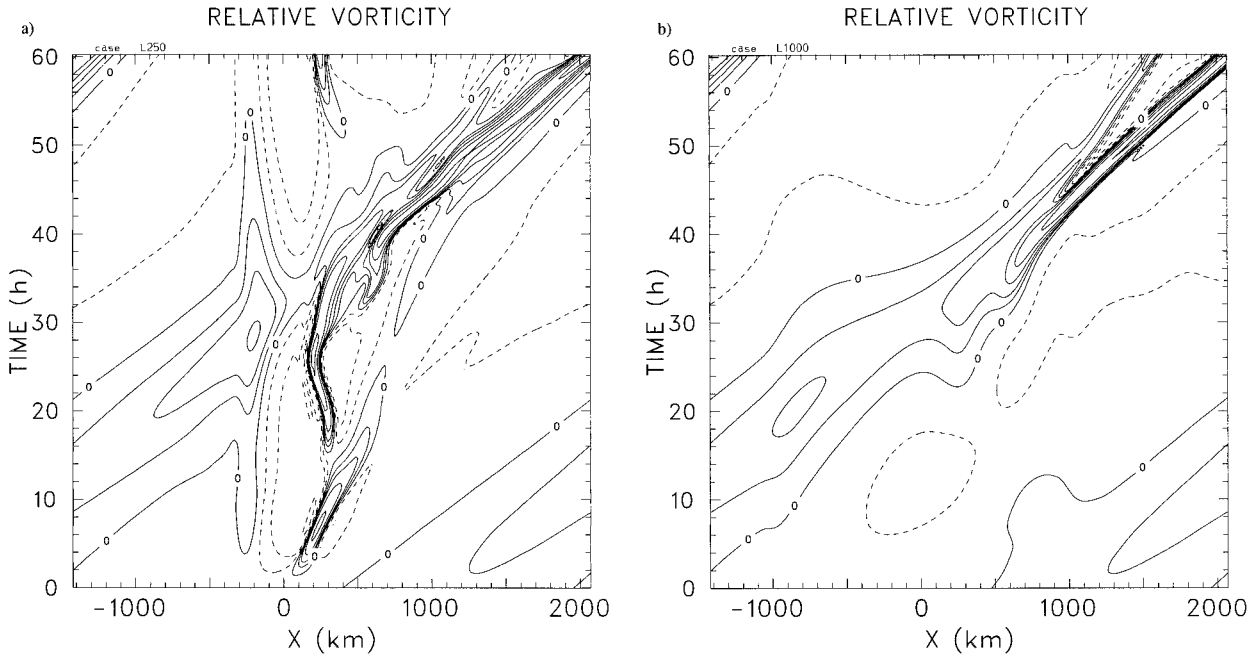

FIG. 11. Time variation of the surface relative vorticity for (a) L250 and (b) L1000. Scaling and contour interval as in Fig. 3a.

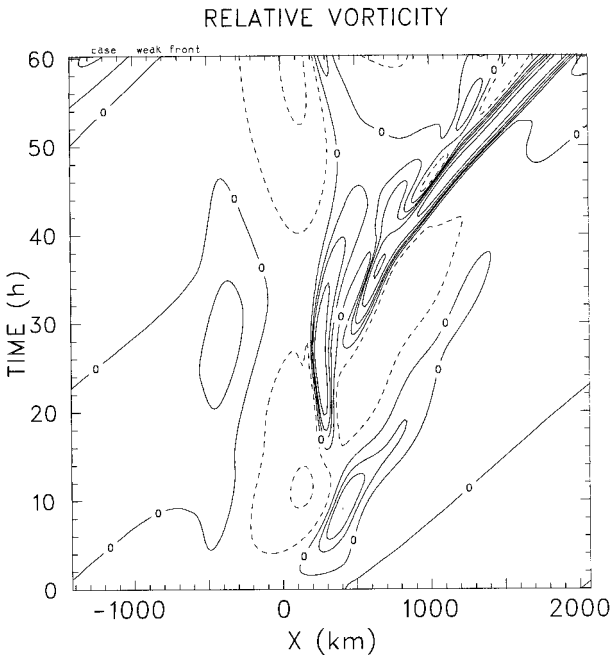

FIG. 12. Time variation of the surface vorticity for the weak front interacting with mountain. Scaling and contour interval as in Fig. 3a.

Grant ATM-9113487. The authors would like to thank Dr. John Molinari, Phil Schumacher, Eric Hoffman, and the anonymous reviewers for their useful comments during the preparation of this manuscript.

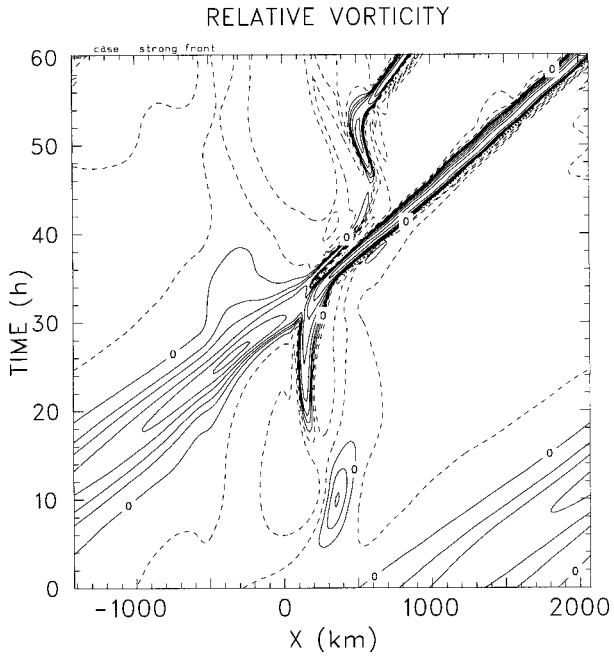

FIG. 13. Time variation of the surface vorticity for the strong front interacting with mountain. Scaling and contour interval as in Fig. 3a.

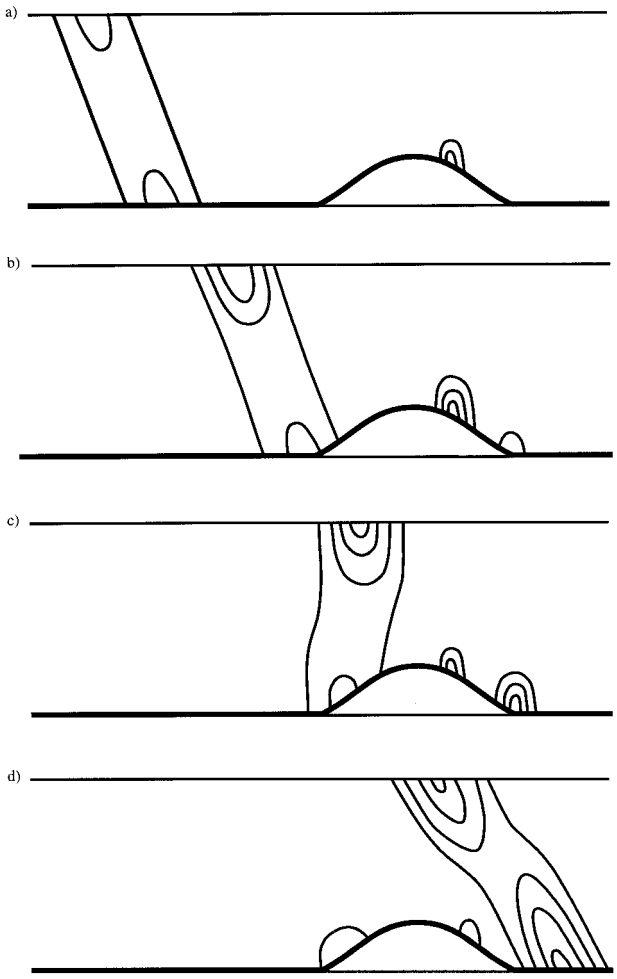

FIG. 14. Idealized schematic of a front propagating over terrain. The schematic shows the low-level blocking of the front along the windward slope, the development of the lee trough and secondary trough along the lee slope, the separation of the upper-level and lower-level frontal waves, and the coupling of the upper-level frontal wave with the secondary trough in the lee of the mountain.

REFERENCES

Anthes, R. A., and T. Warner, 1978: Development of hydrodynamic models suitable for air pollution and other mesometeorological studies. *Mon. Wea. Rev.,* **106,** 1045–1077.

Asselin, R., 1972: Frequency filter for time integrations. *Mon. Wea. Rev.,* **100,** 487–490.

Bannon, P. R., 1983: Quasi-geostrophic frontogenesis over topography. *J. Atmos. Sci.,* **40,** 2266–2277.

——, 1984: A semi-geostrophic model of frontogenesis over topography. *Beitr. Atmos. Phys.,* **57,** 393–408.

——, 1991: Rotating stratified flow over a mountain ridge as an initial value problem. *J. Atmos. Sci.,* **48,** 681–687.

——, and J. A. Zehnder, 1989: Baroclinic flow over a mountain ridge. *J. Atmos. Sci.,* **46,** 703–714.

Bjerknes, J., and H. Solberg, 1922: Life cycle of cyclones and the polar front theory of atmospheric circulation. *Geofys. Publ.,* **3,** 1–18.

Blumen, W., 1988 Stratified, rotating flow over orography: The rigid lid condition and the far-field circulation. *J. Atmos. Sci.,* **45,** 1417–1422.

——, 1992: Propagation of fronts and frontogenesis versus frontolysis over orography. *Meteor. Atmos. Phys.,* **48,** 37–50.
Brown, J., and K. Campana, 1978: An economical time-differencing system for numerical weather prediction. *Mon. Wea. Rev.,* **106,** 1125–1136.
Davies, H. C., 1984: On the orographic retardation of a cold front. *Beitr. Phys. Atmos.,* **57,** 409–418.
Dickinson, M. J., 1995: Frontal interaction with mesoscale topography. Master's thesis, The University at Albany, State University of New York, 265 pp. [Available from The University at Albany, State University of New York, Dept. of Earth and Atmospheric Sciences, 1400 Washington Avenue, Albany, NY 12222.]
Eady, E. T., 1949: Long waves and cyclone-waves. *Tellus,* **1,** 33–52.
Egger, J., 1992: The orographic retardation and deformation of a frontal zone. *Meteor. Atmos. Phys.,* **48,** 131–137.
——, 1995: Interaction of cold-area blocking and upper-level potential vorticity anomalies during lee cyclogenesis. *Tellus,* **47A,** 597–604.
——, and K. P. Hoinka, 1992: Fronts and orography. *Meteor. Atmos. Phys.,* **48,** 3–36.
Gross, B. D., 1994: Frontal interaction with isolated topography. *J. Atmos. Sci.,* **51,** 1480–1496.
Haderlein, K., 1989: On the dynamics of orographically retarded cold fronts. *Beitr. Phys. Atmos.,* **62,** 11–19.
Hartsough, C. S., and W. Blumen, 1990: Objective cross-sectional analysis of diabatic circulations and vertical motions using ALPEX data. *Meteor. Atmos. Phys.,* **43,** 220–230.
Hoinka, K. P., and H. Volkert, 1987: The German front experiment 1987. *Bull. Amer. Meteor. Soc.,* **68,** 1424–1428.
Hoskins, B. J., and F. P. Bretherton, 1972: Atmospheric frontogenesis models. Mathematical formulation and solution. *J. Atmos. Sci.,* **29,** 11–37.
Keuler, K., J. Kerkmann, H. Kraus, and E. Schaller, 1992: Orographical modification and large scale forcing of a cold front. *Meteor. Atmos. Phys.,* **48,** 105–130.
Keyser, D., 1981: Frontogenesis in the planetary boundary layer of an amplifying, two-dimensional baroclinic wave. Ph.D. thesis, The Pennsylvania State University, 295 pp. [Available from The Pennsylvania State University, Dept. of Meteorology, University Park, PA 16802.]
——, 1986: Atmospheric fronts: An observational perspective. *Mesoscale Meteorology and Forecasting,* Peter S. Ray, Ed., Amer. Meteor. Soc., 216–255.
——, and R. A. Anthes, 1982: The influence of planetary boundary layer physics on frontal structure in the Hoskins–Bretherton horizontal shear model. *J. Atmos. Sci.,* **39,** 1783–1802.
Kurz, M., 1990: The influence of the Alps on structure and behavior of cold fronts over southern Germany. *Meteor. Atmos. Phys.,* **43,** 61–68.
Mattocks, C., and R. Bleck, 1986: Jet streak dynamics and geostrophic adjustment processes during the initial stages of lee cyclogenesis. *Mon. Wea. Rev.,* **108,** 427–435.
Merkine, L. O., 1975: Steady finite-amplitude over bottom topography. *J. Atmos. Sci.,* **32,** 1881–1893.
O'Handley, C., and L. F. Bosart, 1996: The impact of the Appalachian Mountains on cyclonic weather systems. Part I: A climatology. *Mon. Wea. Rev.,* **124,** 1353–1373.
Orlanski, I., and B. B. Ross, 1984: The evolution of an observed cold front. Part II. Mesoscale dynamics. *J. Atmos. Sci.,* **41,** 1669–1703.
Pierrehumbert, R. T., and B. Wyman, 1985: Upstream effects of mesoscale mountains. *J. Atmos. Sci.,* **42,** 977–1003.
Schumacher, P. N., D. J. Knight, and L. F. Bosart, 1996: Frontal interaction with the Appalachian Mountains. Part I: A climatology. *Mon. Wea. Rev.,* **124,** 2453–2468.
Schumann, U., 1987; Influence of mesoscale orography on idealized cold fronts. *J. Atmos. Sci.,* **44,** 3423–3441.
Smith, R. B., 1979: The influence of mountains on the atmosphere. *Advances in Geophysics,* Vol. 21, Academic Press, 87–230.
Williams, R. T., M. S. Peng, and D. A. Zankofski, 1992: Effects of topography on fronts. *J. Atmos. Sci.,* **49,** 287–305.
Zehnder, J. A., and P. R. Bannon, 1988: Frontogenesis over a mountain ridge. *J. Atmos. Sci.,* **45,** 628–644.